Materials Advances

PAPER

Check for updates

Synthesis and characterization of core–shell NMC microparticles as cathode materials for Li-ion batteries: insights from *ex situ* and *in situ* microscopy and spectroscopy techniques†

J. García-Alonso,[a] S. Krüger,[b] K. Kelm,[b] E. Guney,[c] N. Yuca,[cd] I. J. Villar-García,[ef] B. Saruhan, [b] V. Pérez-Dieste,[e] D. Maestre*[a] and B. Méndez [a]

The achievement of lithium ion batteries (LiBs) with improved electrochemical performance requires advances in the synthesis of cathode materials with controlled composition and properties. In particular, NMC core–shell materials formed by a Ni-rich core and a Mn-rich shell are recently gaining interest as they allow the achievement of increased energy density and high discharge capacity values. In order to overcome some of the limitations of these NMC compounds and broaden their applicability, controlled synthesis and detailed analysis of their properties are required. In this work, NMC in the form of core and core–shell microparticles have been synthesized by an oxalate-assisted co-precipitation synthesis method which allows control of the final composition. The morphology, crystalline structure and composition of the particles have been investigated as a function of the synthesis parameters and the presence of the Mn-rich shell, by means of diverse microscopy and spectroscopy techniques. Additionally, *in situ* SEM and XPS measurements allow analysis of the NMC particles in variable operation environments. Aspects such as the cationic mixing in the NMC compound or the formation of a rock-salt phase as the annealing temperature increases are discussed. Finally, preliminary electrochemical tests have been performed using NMC particles as cathodes in LiBs.

1. Introduction

In the search for improved electrochemical behaviour and more efficient devices, modern lithium ion batteries (LiBs) increasingly demand higher rate capabilities, stability and long-term cyclability. Among the diverse components of LiBs, the appropriate selection of active cathode materials plays a key role in the development of devices resulting in better electrochemical behaviour and performance. Hence, efforts are invested in the design, synthesis and study of diverse cathode materials.[1–3]

[a] *Departamento de Física de Materiales, Facultad de CC. Físicas, Universidad Complutense de Madrid, Madrid, 28040, Spain. E-mail: dmaestre@ucm.es*

[b] *Institute of Materials Research, German Aerospace Center (DLR, e.V.), Linder Hoehe 51147, Cologne, Germany*

[c] *Enwair Energy Technologies Corporation, Kagithane, Istanbul 34415, Turkey*

[d] *Energy Institute, Istanbul Technical University, İTÜ Ayazağa Kampüsü, Enerji Enstitüsü, 34469 Sarıyer, İstanbul, Turkey*

[e] *ALBA Synchrotron Light Source, Carrer de la Llum 2-26, 08290 Cerdanyola del Vallès, Barcelona, Spain*

[f] *Departamento de Química, Facultad de Farmacia, Universidad CEU San Pablo, Urbanización Montepríncipe, 28668 Boadilla del Monte, Madrid, Spain*

† Electronic supplementary information (ESI) available. See DOI: https://doi.org/10.1039/d4ma00994k

In the last few years, layered lithium and transition metal (TM) oxides in the form of $Li(Ni_xMn_yCo_z)O_2$, known as NMC, are considered as one of the most promising cathodes for the next generation of LiBs based on their high energy density, specific capacity and reduced use of Co.[3,4] NMC compounds exhibit a layered NaFeO crystalline structure with the $R\bar{3}m$ space group in which TMO_2 layers are separated from Li layers by oxygen.[5] In this structure, Li and TM cations are located in the octahedral Wyckoff 3a and 3b sites, respectively. Hence, this layered structure enables Li diffusivity in the Li slab space between strongly bonded TMO_2 layers, which involves improved battery performance. Actually, NMC-based cathodes can outperform conventional $LiCoO_2$ and lithium iron phosphate (LFP) ones in terms of operational voltage, stability during cycling and capacity.[1,2,6] In particular, NMC cathodes with high Ni contents, such as NMC 631, 622, and 811, are gaining increasing attention in the battery market owing to the reduced use of critical Co in combination with the higher discharge capacity, increased energy density and reduced costs.[7] However, increasing the Ni content can involve decreased stability and larger Li/Ni cationic mixing as well, which can deteriorate the electrochemical performance of the layered electrodes. It is commonly

reported that a certain degree of cation disorder is frequently present in Ni-rich NMC materials, owing to the tendency of Ni^{2+} to occupy Li^+ 3b sites due to the similar ionic radii of Li^+ (0.76 Å) and Ni^{2+} (0.69 Å), which eventually limits the Li^+ mobility and rate capability of the layered cathodes and can even produce a phase transition into a non-layered structure. In order to overcome some of the drawbacks related to Ni-rich NMC cathodes, diverse strategies are pursued including the design and development of NMC materials with controlled doping, core-gradients and core–shell structures by cost-effective and scalable methods such as solvothermal, spray-pyrolysis, hydrothermal and solid-state reactions, among others.[8–12]

Different studies have demonstrated the achievement of improved structural and electrochemical performance in LiBs with cathode materials formed by NMC layered oxides in the form of core–shell particles with a Ni-rich core in combination with a Mn-rich shell.[13,14] In that case, the Ni-rich core ensures high specific capacity, while improved structural and thermal stability is provided by the Mn-rich shell. A redesign of the NMCs must be undertaken not only to improve the electrochemical performance but also to widen their applicability in other research fields. Therefore, special attention should be paid during the synthesis and subsequent characterization of core–shell particles for the achievement of the best control of their composition, dimensions and crystalline structure. In that sense, so far in the literature, diverse experimental techniques have been employed in order to achieve deeper knowledge of the crystalline structure and the properties of the Ni-rich NMC materials, including recent *in situ* and *in operando* approaches under variable conditions, such as temperature and humidity,[15–18] which allows the analysis of the materials under operation conditions. A combination of modern approaches by *in situ* techniques, able to reveal real time information on the morphology, microstructure and electronic properties, with more conventional *ex situ* microscopy and spectroscopy techniques can lead to gaining relevant insights into the optimization of the synthesis and subsequent performance of NMC materials. However, the associated investigation of all these aspects, *i.e.* synthesis, microstructure, phase constituents and cathode performance in a LiB, has been commonly missing in the literature.

In this work, for the fabrication of core–shell structures, a two-staged oxalate-assisted co-precipitation synthesis method is employed in order to form cathode particles having a Ni-rich core, NMC 811, and a Mn-rich shell, NMC 631. The co-precipitation route offers advantages to obtaining particles with a homogeneous structure and controlled composition and is a simple and scalable method. For the characterization of these particles various microscopy and spectroscopy techniques have been employed, also including *in situ* analyses which can shed light on the variations in the properties of the probed particles in diverse LiB operation environments. Additionally, LiB coin cells are produced with these synthesised NMC particles in order to carry out preliminary electrochemical tests and to identify the performances of NMC-based electrodes.
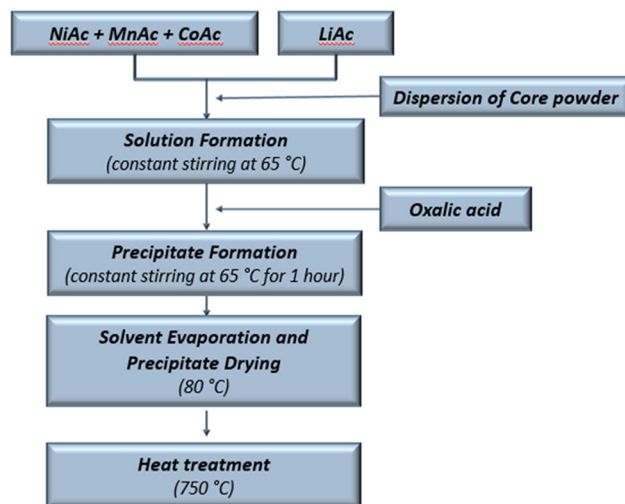

Fig. 1 Flow diagram of NMC core/shell powder synthesis.

2. Materials and methods

This work analyses the core and core–shell NMC microparticles produced by means of a co-precipitation method (Fig. 1). Li-incorporation was carried out simultaneously during the co-precipitation process.

To obtain NMC core particles of the 811 composition (80% Ni, 10% Mn and 10% Co), Ni, Mn, Co and Li acetate solutions were prepared, and co-precipitation of mixed oxide was performed by dropwise addition of oxalic acid solution. The resulting mixture was stirred continuously at 65 °C for 1 hour. Afterwards the obtained precipitate was dried at 80 °C for 2 h, to remove absorbed water, and calcined in air under required heat treatment conditions, as described in Table 1.

To obtain the core–shell structure, the dried NMC core particles were suspended in a mixed metallic solution giving the shell composition with the adequate acetate ratio to achieve the formation of the NMC 631 shell composition (60% Ni, 30% Mn and 10% Co). Oxalic acid was added to this, and all further steps were repeated as those used in the synthesis procedure of core particles. The obtained core–shell precipitate was dried at 80 °C for 2 h and calcined at 750 °C in air for 8 hours. As is known, the lack of oxygen during the synthesis procedure can accelerate degradation mechanisms such as phase transitions or the formation of additional undesired phases, which can significantly impact the quality of the material and, as a result, its battery performance. Therefore, the heat treatment of NMC powders has been performed with constant air circulation in the furnace.

Table 1 List of samples including core and core–shell particles

Sample	Structure (NiMnCo)	Treatment
Core_Pre	Core (811)	—
Core_5	Core (811)	500 °C/8 h
Core_75	Core (811)	750 °C/8 h
Core_9	Core (811)	900 °C/8 h
CS-75	Core (811)/shell (631)	750 °C/8 h

X-ray diffraction (XRD) measurements were performed using PANalytical X′Pert Powder equipment with the Bragg–Brentano geometry using Cu Kα radiation (λ = 1.541874 Å). A FEI-Inspect S50 scanning electron microscope (SEM) and a ThermoFisher-Prisma E-SEM using acceleration voltages in the range of 2–15 kV were employed for the morphological study. *In situ* SEM observation at variable temperatures of up to 750 °C was performed with the ThermoFisher-Prisma E-SEM by using a specific sample holder and cooling/heating stage control with a chamber feedthrough plate for water connections, thermocouple connections and power connections. Energy dispersive X-ray spectroscopy (EDS) analysis was carried out in a Leica 440 Stereoscan SEM equipped with a Bruker AXS 4010 detector and in a ThermoFisher-Prisma E-SEM equipped with an EDS ultra-dry detector, using an acceleration voltage of 18 kV.

A Horiba Jobin-Yvon LabRam HR800 confocal microscope with a He–Ne (λ = 633 nm) laser as an excitation source was employed for micro-Raman spectroscopy measurements at room temperature. Inductively coupled plasma-optical emission spectrometry (ICP-OES) was employed for the detection and semi-quantification of lithium in ARCOS equipment from SPECTRO with an excitation source (ICP, PerkinElmer Optima 3300DV). In that case, three specimens for each sample were analysed to minimize the statistical error in Li quantification. X-ray photoelectron spectroscopy (XPS) measurements were performed at the CIRCE line at ALBA Synchrotron (Spain) using a Near-Ambient Pressure Photoemission (NAPP) endstation which allows *in situ* analysis. A PHOIBOS 150 NAP energy analyzer (SPECS GmbH) was used to analyse the emitted photoelectrons. The source is a pure permanent magnet APPLE II helical undulator and the hemispherical electron energy analyzer is a PHOIBOS 150 NAP from SPECS, with four differentially pumped stages connected by small apertures, which can operate at sample pressures ranging from an UHV up to 25 mbar. The analyzer axis is at 54.7° with respect to the incident beam. The photon flux is $\sim$1023 ph s^{-1} and the analysis spot on the sample is 20 × 100 μm². The energy used was in the 190–1486 eV range in order to assess the electronic properties of the surface of the particles, based on the high surface sensitivity of this technique. Survey scans were acquired using a pass energy of 20 eV and a step size of 1 eV and high-resolution scans were acquired using a pass energy of 10 eV and a step size of 0.1 eV at different dwell times depending on signal to noise ratios. Transmission electron microscopy (TEM) investigations were performed with a Philips Tecnai F30 STEM (Philips, the Netherlands) operating at 300 keV. The microscope was equipped with a Gatan 794 CCD camera (Gatan, USA) and a high-angle annular dark-field (HAADF) detector (Fischione, USA) for scanning transmission electron microscopy (STEM). Furthermore, for energy dispersive electron spectroscopy (EDS), a windowless silicon drift detector (Apollo XLT, EDAX, USA) was installed. For electrochemical measurements, electrodes with a composition of 80% active material, 10% carbon black (Timcal Super C65) and 10% polyvinylidene fluoride (PVDF) were prepared for electrochemical analysis. The electrode sheet was cut into 15 mm diameter

coin cell electrodes. The electrodes were assembled in a 2032 coin cell containing a Li metal counter electrode and a commercial 1 M LiPF6 EC : DEC (50 : 50) electrolyte. Electrochemical impedance spectroscopy (EIS) and cyclic voltammetry (CV) were performed using a Gamry reference 3000 potentiostat/galvanostat. EIS measurements of the prepared electrode were carried out in the range of 1 MHz to 0.1 Hz at a constant current of 10 mA. CV measurement of the electrodes was performed at a scan rate of 1 mV s^{-1} in the range of 2 V to 4.6 V. The galvanostatic charge/discharge (GCD) cycling test was performed using a Neware battery testing system (4000 series model 5 V 50 mA).

3. Results and discussion

3.1. XRD

Firstly, the core particles without a shell were studied by XRD as a function of thermal annealing employed during the synthesis process (Fig. 2). Prior to the application of additional thermal annealing, the XRD pattern of as-synthesized Core_Pre particles showed maxima related to the presence of diverse transition metal (TM) oxalates, based on Ni, Mn and Co, as well as Li oxalate formed during the co-precipitation process which is accompanied with peaks coming from the residual oxalic acid in the precursors.

After annealing at 500 °C, the metal oxalates and oxalic acid disappeared and new XRD maxima related to NiO in the rocksalt phase ($Fm\bar{3}m$) and Li_2CO_3 became visible, as marked in the diffractogram from Core_5. Based on the profile of the XRD maxima, contributions associated with spinel phases ($Fm\bar{3}m$) are also considered for this sample, as confirmed by the presence of the peak at 18.7° related to spinel oxides based on Ni, Mn and Co. It is only when the temperature of the thermal treatment is increased up to 750 °C that XRD maxima
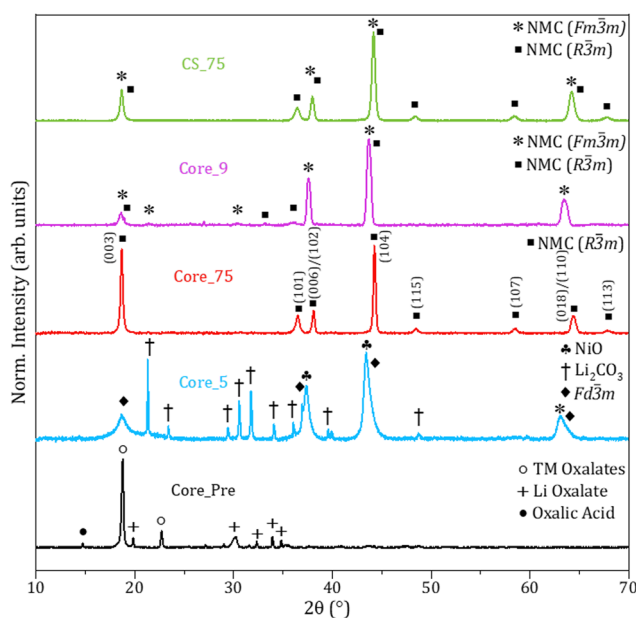

Fig. 2 XRD patterns from core and core–shell samples.

related to the presence of Li(Ni$_x$Mn$_y$Co$_z$)O$_2$ compounds corresponding to the $R\bar{3}m$ group, named NMC, are observed in the XRD patterns, as indicated in Fig. 2. In that case, peaks associated with Li$_2$CO$_3$ are not observed in the XRD patterns. Expectedly, the increase of temperatures higher than 725 °C leads to the decomposition of these Li-based compounds.[19] The diffractogram from Core_75 exhibits intense and well-defined maxima dominated by (003) and (104) reflections from NMC layered $R\bar{3}m$. In this case, XRD signals corresponding to spinel oxides, lithium carbonate and other related compounds are not detected, within the resolution of the technique, and therefore XRD patterns confirm the achievement of well-crystallized NMC compounds in these samples.

Finally, thermal annealing at 900 °C induces the formation of a rock-salt phase in addition to the NMC layered phase for the sample Core_9, as higher cation diffusion and mobility are induced at this temperature leading to the formation of Ni-rich rock-salt domains in the NMC compounds. It should be considered that the formation of a rock-salt phase in NMC-based cathodes employed in LiBs can induce lower electrochemical behaviour during cycling. Additionally, a very reduced peak such as the one at 27.0° can also be associated with the formation of highly Li doped areas indexed to the orthorhombic phase of Li$_2$NiO$_2$.[20]

Based on these XRD measurements, it is outlined that the optimization of the NMC synthesis requires thermal annealing at 750 °C, otherwise the segregation of a Ni-rich rock-salt phase is promoted at higher temperatures. Therefore, annealing at 750 °C was preferred to be employed during the synthesis of core–shell particles analysed in this work. The XRD pattern from the core–shell sample CS_75 is also dominated by maxima related to NMC, as shown in Fig. 2. However, in this case (104) maxima from $R\bar{3}m$ dominates the diffractograms, contrary to the XRD signal from the counterpart core–particles (Core_75) where higher relative intensity was observed for the (003) maxima. Added to this, some maxima from the core–shell sample are wider than those from the core samples treated at 750 °C, which could indicate the presence of a Ni-rich rock-salt phase ($Fm\bar{3}m$), although in a lower amount as compared to Core_9 particles.

According to the literature, the ratio of the (003) and (104) reflections, I_{003}/I_{104}, can be related to the Ni and Li cation mixing and the associated lattice disorder in the $R\bar{3}m$ layered NMC compound.[5] It is commonly accepted that Ni^{2+}/Li$^+$ mixing, and hence cationic disorder, increases with higher Ni content in the NMC lattice. Despite the fact that this aspect and the mechanisms underlying cationic exchanges are still under debate, low I_{003}/I_{104} values are commonly associated with structural deviations from NMC layered towards cubic symmetry. The disordered phases commonly involve lower Li diffusivity and worse electrochemical behaviour as cathodes in LiBs. Besides, the splitting of the (006)/(102) and (018)/(110) reflections can be associated with a well-layered crystalline NMC structure. In this work, changes in the I_{003}/I_{104} ratio have been appreciated among the samples; however, splitting of the (006)/(102) and (018)/(110) peaks is hardly noticeable. According to the XRD results shown in Fig. 2, the sample Core_9 treated at a high temperature of 900 °C

shows lower I_{003}/I_{104} values than Core_75 samples, together with the presence of a rock-salt structure, which could involve a $R\bar{3}m$ layered lattice disordered towards cubic $Fm\bar{3}m$ promoted by high-temperature annealing. Previous works also reported increased cationic migration between Li and TM slabs leading to the formation of a NiO rock-salt phase with high content of Mn and Co promoted at high temperatures.[16,21] These results confirm that, despite the fact that thermal treatments are required to achieve a layered NMC structure, temperatures higher than 750–800 °C should be avoided during the proposed synthesis route in order to inhibit the formation of a rock-salt structure, as observed in Core_9 samples.

Due to the possible presence of various phases in the samples treated at 750 °C, especially for the core–shell sample, Rietveld refinements were performed in this work, as they allow for a more in-depth analysis of the (003) to (104) relative intensity ratio. The refinement results from samples Core_75 and CS_75 are presented in Fig. S1 (ESI†), while the parameters obtained from the Rietveld refinement are included in Table S1 (ESI†). Rietveld refinement results confirm that sample Core_75 consists of a single phase NMC layered oxide ($R\bar{3}m$) structure, as expected from the cationic ratio used during synthesis. On the other hand, an additional rock-salt Ni-rich phase should also be considered, in combination with the NMC one, in the analysis of the CS_75 core–shell sample. Similar lattice parameters are estimated for the NMC compounds both for the core and the core–shell samples, although slightly larger a and c values, as well as c/a ratio, are observed for CS_75. In addition, the interslab distance in the TM slab ($d_{\text{M–O Vert.}}$) decreases for the CS_75 sample in the vertical direction probably due to the variations in the cationic ratio. Based on the Rietveld refinement, core–shell particles exhibit notably lower Ni (3a) occupancy in the layered $R\bar{3}m$ structure, and hence reduced cationic mixing, as compared to Core_75 (Table S1, ESI†). This is in accordance with the expected presence of the shell portion at the core–shell microparticles with a cationic ratio of 631 and hence a lower Ni content, although the presence of Ni^{3+} which reduces Ni migration to Li slabs should also be considered. The notable Ni migration to the Li (3a) positions observed for the core sample might be directly related to the use of a high Ni content to obtain the NMC 811 composition while the CS_75 particles present a much lower Ni migration. Ni-rich NMC compounds are known to present a much higher possibility for Ni migration to the Li positions especially when treated at high temperatures compared to their counterparts presenting less Ni content.[16,22]

3.2. SEM

SEM analysis was employed to study the dependence of the morphology and dimensions of the particles on the synthesis parameters. Particles of the Core_Pre sample exhibit an irregular appearance and variable size distribution with average dimensions of around 2 μm, as shown in Fig. 3a. The surface of these microparticles shows a grainy appearance with irregular roughness. According to the corresponding XRD patterns, these irregular particles should mainly consist of transition metal oxalates with a lower amount of Li oxalate and oxalic acid.
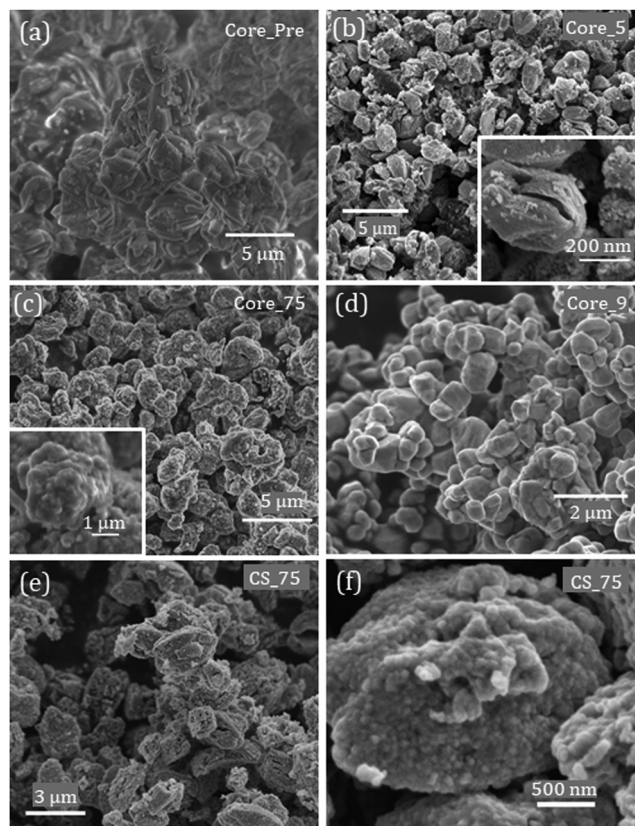
Fig. 3 SEM images from core samples (a) Core_Pre, (b) Core_5, (c) Core_75, (d) Core_9, and (e) and (f) the core–shell sample CS_75.

Particles of the Core_5 sample, heat-treated at 500 °C, show a more homogeneous rounded appearance with smoother surfaces and lower average dimensions down to 1.5 μm (Fig. 3b), as compared to the Core_Pre ones. Occasionally, Core_5 microparticles exhibit cracks at their surface, as observed in the inset in Fig. 3b, together with regions with variable contrast which could be associated with residues from the chemical synthesis, in agreement with the XRD analysis.

The cracks can be related to volume changes that occurred during the formation of the oxides and spinel compounds. Upon increasing the temperature up to 750 °C, the Core_75 particles, which should consist of NMC compounds based on the corresponding XRD results, show slightly higher average dimensions of 1.8 μm and surfaces with a grainier appearance, as observed in Fig. 3c. Finally, treatment at 900 °C increases the surface roughness and the grainy appearance of the microparticles of the Core_9 sample, the surface of which is formed by groups of small grains of around 500 nm, some of which exhibit a faceted appearance. The formation of Ni-rich rock-salt at 900 °C, confirmed by XRD, should be related to the morphological variations observed at the surface of these particles (Fig. 3d).

Regarding the core–shell sample CS_75 treated at 750 °C, the microparticles show average dimensions of 2.2 μm (Fig. 3e), which represents an increase in size of 300–400 nm as compared to the Core_75 core particles treated at the same temperature.

Furthermore, the surface of these core–shell particles exhibits a more porous appearance (Fig. 3f) as compared to the grainy surface of the Core_75 particles. This increase in the dimensions together with the promoted porous surface can be possibly related to the NMC 631 shell formation in the core–shell particles.

In order to gain deeper insights into the influence of the thermal treatment on the core and core–shell particles, *in situ* SEM analysis at temperatures up to 750 °C was carried out, leading to an innovative approach to study the diverse steps occurring during thermal treatment. Dried Core_Pre particles have been placed in an environmental SEM which allows control of the temperature and pressure conditions during SEM observation. In this case, the temperature was increased up to 750 °C at a rate of 10 °C min^{-1} and then maintained at 750 °C for 3 hours, to replicate the intermediate steps during the formation of the particles. Multiple sets of particles have been studied in the SEM following this process in order to assess changes in their morphology promoted during heating. Representative results are shown in Fig. 4.

SEM images show an initial decrease in the dimensions of the particles as the temperature increases, with a drastic change occurring at 500 °C, as observed in Fig. 4a and b, where a reference particle has been marked with a circle. This volume contraction, which in some cases is accompanied by changes at the surface of the particles, is in agreement with the lower sizes of the particles from sample Core_5 as compared to Core_Pre (Fig. 3), and could be related to the oxidation of the TM oxalates to spinel and NiO, as confirmed by XRD, as well as dehydration and crystallization effects promoted by temperature. The continuous temperature increase from 500 °C to 750 °C only induces slight changes in the final size of the NMC particles, as compared to the particles annealed at 500 °C (Fig. 4b and c). Variations at the surface of the particles are also noticed as a function of thermal annealing. In addition to higher surface roughness, some cracks are observed in the particles treated at higher temperatures, as marked with an arrow in Fig. 4a and b, possibly due to the volume changes that occurred during this process. These cracks are in agreement with those observed in the Core_5 particles (Fig. 3b), which can be related to the volume contraction that occurred at 500 °C. Similar phenomena are observed in the *in situ* SEM study of core–shell particles, included as the ESI† (Fig. S2).

3.3. Compositional analysis

Compositional analysis of the microparticles has been carried out by EDS and ICP-OES. Regarding Li detection and
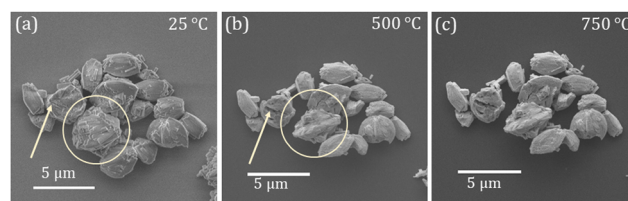

Fig. 4 *In situ* SEM images of the Core_Pre sample (a) without annealing and by annealing at (b) 500 °C and (c) 750 °C.

quantification, ICP-OES is required as this light element cannot be detected by conventional EDS.

The analysis of the averaged EDS spectra acquired at diverse regions of the probed samples indicates that the particles are formed by Ni, Mn, Co and O, with a variable presence of C in some samples, within the resolution of the technique.

Similar EDS spectra have been obtained among the different probed regions in each sample which confirms the compositional homogeneity of the particles and the lack of clusters or regions with significant variable composition. Fig. 5 shows two representative EDS spectra acquired on the samples Core_75 and CS_75 where variations in the presence of the elements can be clearly observed. In particular, a higher presence of Mn is detected in CS_75 as compared to Core_75, as expected due to the presence of a Mn-rich shell in the former. The average composition values estimated from the EDS analysis, together with the Ni/Mn/Co ratio from each sample, are included in Table 2. The amounts of oxygen and carbon, not shown in Table 2, are higher in the particles from the Core_Pre sample, where NMC is not yet formed and the presence of residues from the synthesis has been confirmed by XRD. After thermal treatments, Core-5, Core_75 and Core_9 samples exhibit a similar Ni/Mn/Co ratio around the expected 8/1/1. A further decrease in the oxygen content is observed for the Core_9 sample.

Regarding the core–shell particles, the average amount of Ni decreases in CS_75 particles, as compared to the core samples, leading to a Ni/Mn/Co ratio closer to the 6/3/1 value expected for the Mn-rich shell. The deviations of the 6/3/1 shell composition can be explained based on the micrometric penetration depth of the EDS technique which involves the Ni-signal both from the shell and the Ni-rich core regions of the particles. The core–shell formation was also studied in the CS_75 particles by means of EDS line scans, as shown in the ESI† (Fig. S3). An increase in Ni is observed towards the centre of the particles, in combination with the corresponding increase in Mn near the edges, which indicates the formation of a Ni-rich core and Mn-rich shell composition.

According to the EDS-SEM measurements, the average thickness of the shell is approximated to be around 350 nm in particles with average sizes around 2 μm.

Table S2 (ESI†) includes the Li, Ni, Mn, and Co contents, as well as the corresponding Ni/Mn/Co ratio, estimated from the ICP-OES study. In this case, only core and core–shell samples treated at 750 °C, Core_75 and CS_75, have been analysed as representative samples with the NMC crystalline structure.

Table 2 Atomic% concentrations and the corresponding Ni/Mn/Co ratios of core and core–shell samples, based on EDS analysis

Sample	Ni (at%)	Mn (at%)	Co (at%)	O (at%)	Ni/Mn/Co
Core_Pre	11.7 ± 0.6	1.3 ± 0.1	1.2 ± 0.1	85.8 ± 4.6	8.2/0.9/0.8
Core_5	32.2 ± 0.9	3.4 ± 0.1	3.3 ± 0.1	61.2 ± 2.6	8.3/0.9/0.8
Core_75	31.5 ± 1.1	4.1 ± 0.1	3.7 ± 0.1	60.5 ± 3.0	8.0/1.1/0.9
Core_9	43.6 ± 1.3	6.0 ± 0.2	5.6 ± 0.2	44.7 ± 1.7	7.9/1.1/1.0
CS_75	27.1 ± 1.1	9.9 ± 0.4	3.2 ± 0.2	59.8 ± 3.6	6.7/2.5/0.8

Contrary to the EDS analysis, the signal from ICP-OES corresponds to the whole particle including core and shell regions, without surface sensitivity distinction. ICP-OES confirms the presence of Li in all the probed samples. Both core and core–shell particles show a Li concentration around 37–39 at%, although slightly larger values are observed for the core particles. According to the obtained results, the in-bulk Li infiltration approach allows the effective incorporation of Li ions into the NMC structures. Besides, Ni/Mn/Co ratio values estimated from ICP-OES (Table S2, ESI†) are in agreement with those obtained from EDS. However, higher deviations from the expected 6/3/1 values from the shell are observed in the compositional ratio from the CS_75 sample, as in that case the ICP-OES signal is related to the whole particle leading to a higher Ni contribution from the core region, as compared to the EDS analysis.

Finally, the formation of a Mn-rich shell around a Ni-rich core has been confirmed by TEM and EDS investigations of the core–shell NMC powders CS_75, after focused-ion beam (FIB) preparation, as observed in Fig. 6. Compositional images acquired with the Ni, Mn, and Co signals, as well as combined
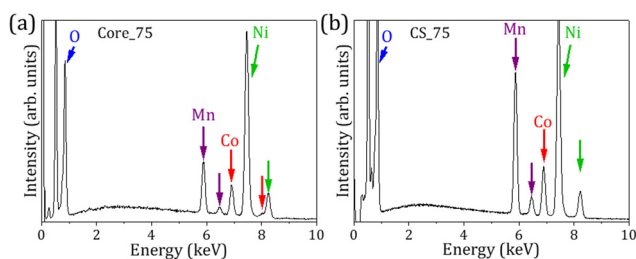

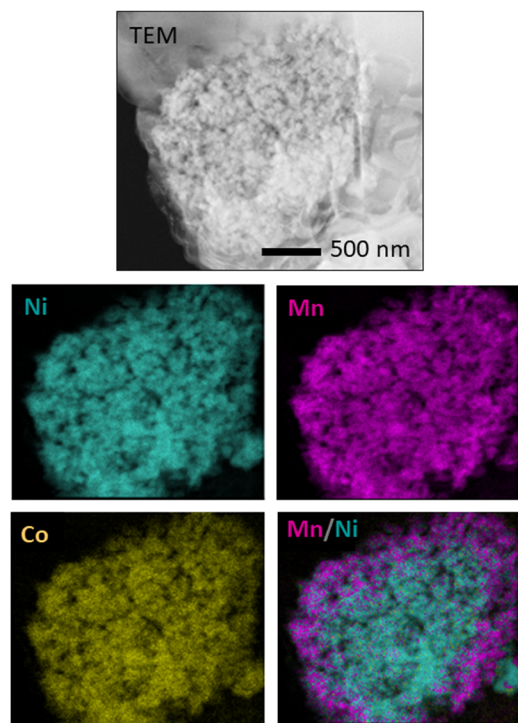**Fig. 5** EDS spectra of (a) Core_75 and (b) CS_75.

Fig. 6 TEM-EDS study of a Ni-rich core/Mn-rich shell particle.

Mn–Ni signals corresponding to the TEM image from a CS_75 particle, are shown in Fig. 6. Based on the TEM-EDS measurements, shell dimensions of around 300–320 nm are estimated in the probed particles with a size of around 1.9 μm, in agreement with the SEM-EDS analysis (Fig. S3, ESI†).

3.4. Raman spectroscopy

Micro-Raman spectroscopy measurements have been carried out to study the vibrational modes of the layered $R\bar{3}m$ structure in NMC microparticles and analyse the presence of other crystalline phases. As no large variations in the Raman signal were observed during the analysis, in agreement with the EDS compositional homogeneity, averaged Raman spectra from the probed samples are shown in Fig. 7. Adequate filters were used to reduce the power of the laser in order to avoid any possible phase transition during Raman signal acquisition.[23]

Raman spectra acquired with a red laser are shown in Fig. 7a. All the spectra are dominated by a signal centred at around 550 cm^{-1}, although some variations in the Raman signal are observed among the probed samples. Contributions to the Raman signal associated with TO and LO modes from rock-salt NiO,[24,25] in combination with vibrational modes from spinel phases ($Fd\bar{3}m$)[26,27] and NMC compounds ($R\bar{3}m$) are observed in Fig. 7a, in agreement with XRD results (Fig. 2).

The analysis of the Raman spectra is not straightforward as in most cases these contributions overlap and are not easily identified. Actually, despite the fact that Raman spectroscopy is a powerful technique to characterize the local structure of NMC compounds, Raman studies based on NMC are scarce as vibrational modes from layered $R\bar{3}m$, spinel oxides and rock-salt can be found in a similar range of wavenumbers which hinders their study and can lead to misleading and controversial conclusions. In this work, deconvolution of the Raman signal from NMC samples in Lorentzian components has been carried out in order to shed light on the understanding of the vibrational modes of the samples under study.

It is commonly accepted that NMC compounds present six active vibrational modes as pairs of A_{1g} and E_g Raman modes associated with each of the TM cations at 3b positions in the $R\bar{3}m$ layered structure.[22,28] E_g vibrational modes can be related to TM–O stretching in the TM slab, while A_{1g} modes are usually associated with TM–O–TM vibrations between TM cations and oxygen located in the interslab space along the c-axis of the $R\bar{3}m$ structure.

As some of the TM cations in NMC present similar mass, especially Ni and Co, the identification of the Raman modes still remains under debate, although for a given cation the wavenumber of the A_{1g} modes is usually higher than for E_g modes. Based on space group theory and previous works,[22,29–31] in this case six Raman modes have been considered in the analysis of the Raman signal from NMC, named $Ni(E_g)$, $Co(E_g)$, $Co(A_{1g})$, $Ni(A_{1g})$, $Mn(E_g)$ and $Mn(A_{1g})$, from lower to higher frequencies. Owing to the lower mass from Mn, the $Mn(E_g)$ and $Mn(A_{1g})$ modes are located at higher frequencies. Fig. 7b shows Raman spectra and the corresponding deconvolutions from samples Core_75 and CS_75, as representative examples of core and core–shell particles. In the analysis of the Raman signal from Core_75 particles, only six active modes from NMC have been considered, while LO modes from the rock-salt phase were also considered in the study of the Raman signal from core–shell particles from the CS_75 sample, based on the corresponding XRD results (Fig. 2). The details of the components considered in the deconvolutions are included as the ESI† (Table S3). Contributions related to $Mn(A_{1g})$ and $Co(A_{1g})$ dominate the Raman signal from Core_75, where $Co(E_g)$ and $Mn(E_g)$ also exhibit relevant contributions, as reported in similar works.[22] On the other hand, the relative intensity of $Mn(A_{1g})$ and $Mn(E_g)$ increases for the CS_75 particles while the relative areas of the $Ni(A_{1g})$ and $Ni(E_g)$ modes are reduced, compared to the deconvolution of the signal from Core_75. This can be directly attributed to the Ni reduction and Mn increase associated with the compositional variation in these samples. Additionally, for the CS_75 sample, the analysis of the deconvolution parameters needs to include an additional LO mode from the Ni-rich rock-salt phase, indicated in Fig. 7b, in agreement with XRD results. The relative areas of the Co modes in the CS_75 sample are slightly reduced as compared to those of Core_75. Variations in the position of the different Raman vibrational modes are also observed between samples. Among other factors, these shifts can be associated with the variations in the distance between the transition metal cations and the oxygens inside the layered structure either inside of the transition metal slabs ($d_{M–O\ Int.}$), E_g, or between slabs ($d_{M–O\ Vert.}$), A_{1g}, already observed through the Rietveld refinements (Table S1, ESI†). When comparing the core and core–shell signals the position of the E_g vibrational modes of the three cations remains nearly unshifted as expected from the similar M–O intraslab distances. In the case of the A_{1g} modes an increase in the wavenumber is observed for the CS_75 sample, possibly associated with the reduction in the interslab distance ($d_{M–O\ Vert.}$), as compared to Core_75. Additionally, effects related to defects and strain can be also considered in the analysis.

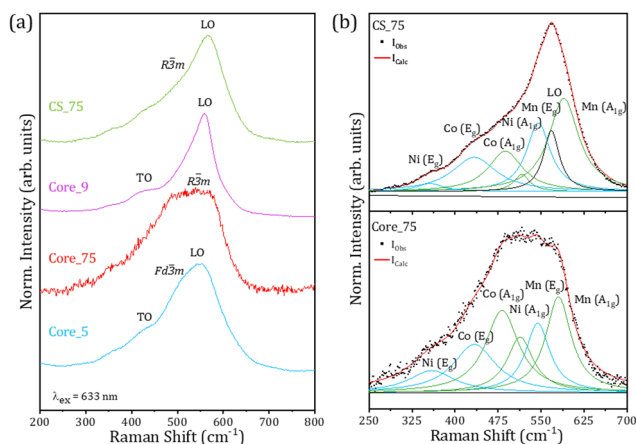Fig. 7 (a) Averaged Raman spectra obtained on the core and core–shell particles using a red laser (λ_{ex} = 633 nm). (b) Deconvolution of the Raman signal from samples Core_75 and CS_75.

3.5. APXPS

Ambient Pressure XPS (APXPS) measurements have been performed at the CIRCE beamline using photon energies in the range of 190–1486 eV to assess the electronic properties of the surface of the particles, based on the high surface sensitivity of this technique. In this case, XPS spectra were acquired only on the CS_75 sample, which exhibits a clear layered NMC composition and core–shell structure (811-631) as expected, together with a low amount of rock-salt phase. Prior to XPS analysis, the powder was pressed into pellets in order to ease the study. XPS spectra were calibrated using the C 1s peak at 284.6 eV from adventitious carbon, while Shirley background corrections and Voigt functions were used for the fitting of the XPS signal. Fig. 8 shows core levels from Ni 2p, Mn 2p, Co 2p, O 1s, and Li 1s acquired under UHV and room temperature conditions. Core levels shown in Fig. 8 are similar to some others reported in the scientific literature for NMC compounds,[32–35] which supports the presence of this layered compound at the surface of the probed particles. Ni 2p core levels, shown in Fig. 8a and measured with a photon energy of 1486 eV, are dominated by contributions at 854.7 and 856.0 eV associated with Ni^{2+} and Ni^{3+}, respectively, in the NMC compound.[34,35] Both contributions exhibit similar relative intensities. Satellite peaks were also considered during the deconvolution of the XPS spectra at 861.2 and 863.3 eV. In this case, a simplified fitting method has been used to illustrate the variation in the Ni^{2+}/Ni^{3+} ratio
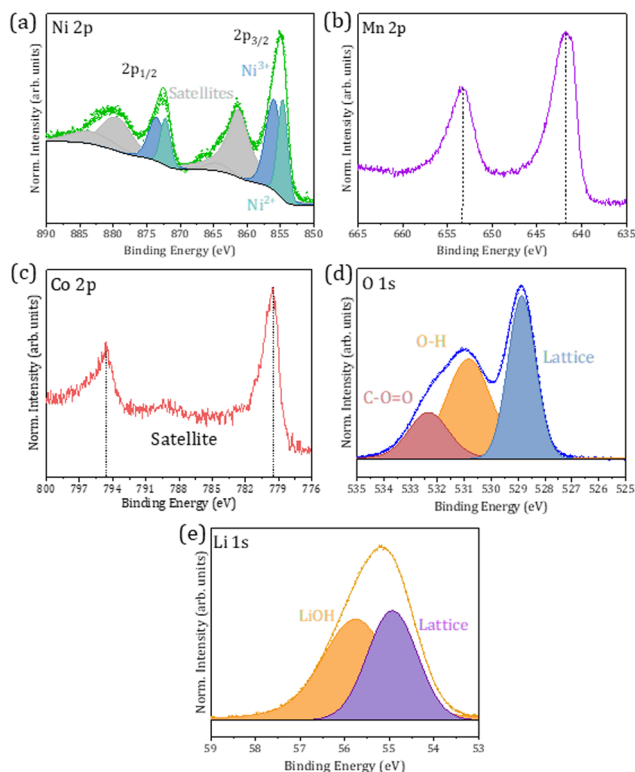

Fig. 8 XPS spectra from (a) Ni 2p, (b) Mn 2p, (c) Co 2p, (d) O 1s and (e) Li 1s core levels acquired under UHV and room temperature conditions for the CS_75 sample.

providing a qualitative description. Quantitative information would require a more complex fitting. Besides, the fitting of the Ni 2p core level does not require the inclusion of an additional contribution at lower binding energies related to Ni in the NiO rock-salt lattice. As this phase was detected by XRD and micro-Raman, and based on the higher surface sensitivity of the XPS technique, this fact could be related to the lack or reduced presence of a Ni-rich rock-salt phase at the surface of the probed particles. Besides, the notable presence of Ni^{3+} at the surface of the particles can decrease Li^+/Ni^{2+} cationic mixing, thus improving Li migration and, as a consequence, the possible electrochemical behaviour. Fig. 8b shows Mn 2p core levels measured with a photon energy of 984 eV, in which the close proximity of the Mn^{3+} and Mn^{4+} contributions, only separated by 0.3 eV, usually hinders the identification of the oxidation state in the NMC compounds.[32] The positions of the $2p_{3/2}$ and $2p_{1/2}$ peaks at 641.7 and 653.3 eV, respectively, in combination with the multiplet splitting observed for the Mn 3s core level, not shown here, suggest a dominant Mn^{4+} oxidation state in the probed samples, in agreement with other authors.[33,36] In this case, the employed photon energy allows avoiding the Auger Ni_{LM2} contribution in this range of energies, which facilitates the study. The presence of Mn^{4+} at the surface of the particles can stabilize the NMC structure during long-term cycling. Co 2p core levels, measured with a photon energy of 984 eV, as shown in Fig. 8c, exhibit dominant contributions at 779.5 and 794.6 eV which can be related to mixed Co^{3+}/Co^{4+} states in the layered NMC compounds.[34,37] A majority of Co^{3+} states can be assumed due to the signal similar to that of $LiCoO_2$ which presents a dominant Co^{3+} oxidation state.[32,38] The presence of Co with mixed valence states at the surface of NMC compounds is commonly reported in the literature. The O 1s XPS signal, measured with a photon energy of 984 eV, is mainly formed by three contributions at 528.9, 530.8 and 532.3 eV commonly associated with oxygen in the NMC lattice, –OH and C–O contributions, respectively. In this case, the contribution from lattice oxygen dominates the XPS spectrum (Fig. 8d).

XPS measurements confirm the effective incorporation of Li ions into the NMC structures by in-bulk Li infiltration during the synthesis (Fig. 8e). Previous ICP-OES results (Table S2, ESI†) determined the presence of Li in the particles, without surface sensitiveness. In this case, XPS measurements acquired with a photon energy of 190 eV confirmed that Li is present at the surface of the probed CS_75 particles. In particular, two main contributions are observed in the Li 1s signal at 54.9 and 55.8 eV which can be related to Li in the NMC lattice, together with LiOH compounds, respectively.[39] The dominant contribution at 54.9 eV confirms that Li has been introduced in the NMC lattice, in agreement with XRD, ICP-OES and Raman spectroscopy analyses, and it is present at the surface of these core–shell particles. Besides, some works also reported the tendency of Li at the upper atomic layers of NMC to interact with H through a Li^+/H^+ exchange mechanism leading to LiOH formation, as observed in this case.[40,41]

In order to investigate the evolution of the surface of the samples under heating and humidity environments, APXPS

measurements have been performed. Variable temperature and atmosphere conditions have been selected during the analysis in order to study the evolution of the XPS signal under heating and humidity environments, to mimic potential LiB operation conditions. These variables can affect the electrochemical behaviour of the LiBs based on NMC cathodes during battery operation.

In this work, Ni 2p, O 1s and Li 1s core levels have been analyzed at room temperature and 500 °C, either under UHV or O_2 atmosphere (1 mbar), as shown in Fig. 9. XPS results from Mn 2p and Co 2p are included as the ESI† (Fig. S4), as lower variations in the XPS signal are observed for those elements during *in situ* XPS measurements.

In particular, annealing at 500 °C promotes an increase in the Ni^{2+}/Ni^{3+} ratio of the samples, both under UHV and O_2 (Fig. 9a). In that case, a possible presence of Ni–OH and/or $NiCO_3$ compounds could be also considered, as Ni-rich NMC compounds present high reactivity for Ni cations at the surface.[41] More noticeable variations are observed in the O 1s during *in situ* observation (Fig. 9b), as expected. In this case, contributions at a higher binding energy of around 532.3 eV associated with carbon species and oxygen deficiency increase their relative intensity as the temperature of the sample increases up to 500 °C under UHV, which can be due to adventitious carbon from the sample and/or outgassing of the sample holder, as well as the formation of oxygen vacancies, as this increase is not observed under an O_2 atmosphere. Expectedly, –OH contributions are also promoted under an oxidizing atmosphere, mainly at 500 °C, as shown in Fig. 9b. Strong variations in the Li 1s signal are also observed during *in situ* analysis, as shown in Fig. 9c. The Li–OH contribution is promoted at high temperature and under an oxidizing atmosphere, as expected. Furthermore, a new significant contribution at a higher binding energy of around 57.7 eV, commonly related to Li_2CO_3, appears in the XPS spectra from the samples treated at 500 °C, mainly under UHV conditions. The increase of the presence of the Li_2CO_3 compound for the samples treated at 500 °C points to possible surface segregation of Li promoted at high temperatures in combination with carbon desorption.

Therefore, high temperature and oxidising conditions can promote the formation of hydroxide and carbonated compounds, mainly related to Li and Ni-based compounds, at the surface of the particles. On the other hand, the stability of the spectra of the three transition metal cations under different temperature and atmospheric conditions suggested good stability of the NMC compound within the parameters considered in *in situ* analysis. These aspects should be considered while optimizing the potential electrochemical behaviour of these NMC particles, being part of LiBs.

3.6. Electrochemical performance

Both Core_75 and CS_75 powders were selected for preliminary electrochemical performance tests based on their above-mentioned in-depth analysis. These NMC powders were employed in the electrodes of coin cells for their analysis.

Initially, the electrochemical analysis of Core_75 NMC811 powders was performed. Electrochemical impedance spectroscopy (EIS) of the Core_75 half-cell was measured before and after cyclic voltammetry (CV) analysis (Fig. 10a). It was found that the charge transfer resistance of Core_75 before CV was 111.8 Ω, and the charge transfer resistance of the electrode decreased to 13.36 Ω after CV due to the current flowing into the cell during CV which activated the internal ion movement of the cell. The cyclic voltammetry results at a rate of 0.1 mV s^{-1} is shown in Fig. 10b. According to CV measurement, Core_75 particles showed the oxidation peak of transition metal ions at 3.95 V in the first cycle. Following the first cycle, this oxidation peak reduced to 3.85 V in the second cycle and continued to decrease. The reduction peak started at 3.57 V and continued to decrease with each step.

The operating voltage range of the Core_75 half-cell was determined in the range of 4.2–2 V by CV measurement and the galvanostatic charge–discharge (GCD) test was performed. Fig. 10c shows the first cycle at the formation step. The specific capacity–voltage graph of the GCD test result showed a low coulombic efficiency of 68%. After the formation step, the first 6 cycles of which are shown in Fig. 10d (3 cycles @C/25 and 3 cycles @C/10), the GCD test was continued @C/5. The Core_75 particles' half-cell showed 77.9% capacity retention after 200 cycles. Even though the capacity retention of the cell was promising, the specific capacity of the material was low compared to some of the literature-based results of NMC811.[42]

The same electrochemical investigation was also carried out for the CS_75 material based on core–shell NMC particles.
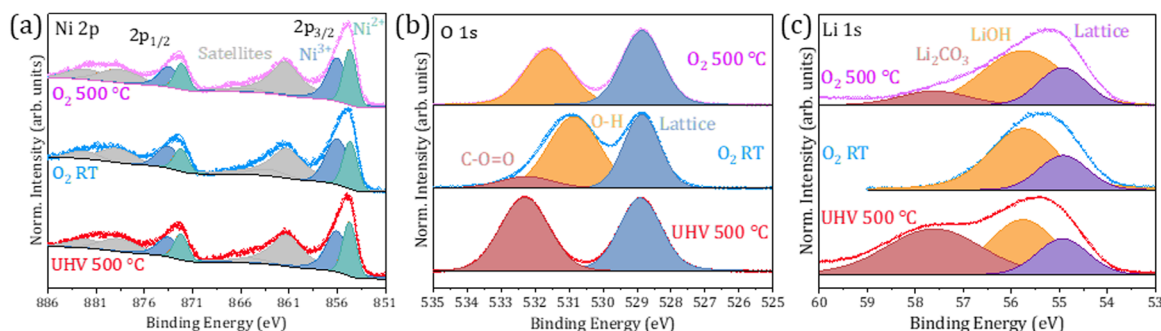

Fig. 9 *In situ* XPS spectra of (a) Ni 2p, (b) O 1s and (c) Li 1s core levels acquired under UHV at 500 °C, and under an O_2 atmosphere at room temperature and 500 °C.
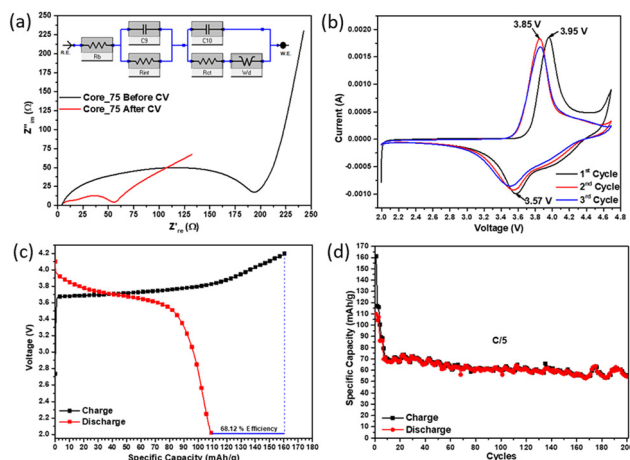
Fig. 10 Electrochemical analysis of the Core_75 sample (a) before CV and after CV EIS spectra comparison. (b) CV analysis. (c) First formation cycle coulombic efficiency result. (d) GCD test result at 0.2C starting from the formation test.

EIS analysis showed that the electrode formed by CS_75 particles exhibited higher resistance before the CV measurement as shown in Fig. 11a. However, after the CV measurement, it was observed that the overall impedance decreased, and most of it was due to the cathode–electrolyte interface (CEI). This means that due to the core–shell structure, high interfacial resistance occurs between the electrode and the electrolyte (1 M LiFP6 EC : DEC (50 : 50)) before any current flows into the cell. CV results in Fig. 11b show that the operating voltage is stabilized after shell coating compared to the Core_75 electrode. Although the oxidation voltage of the electrode formed by CS_75 particles decreased by 0.05 V compared to Core_75, no decrease in oxidation voltage was observed in subsequent cycles. Like the oxidation step, the reduction voltage also decreased by 0.05 V, but the electrode reduction voltage became more stable compared with the Core_75 electrode. The rate capacity test was performed to investigate the specific capacity of the CS_75

cathode material at high C rates (Fig. 11c). A highly irreversible capacity loss (58% coulombic efficiency) was observed in the first cycle of the velocity–capacity test at C/25. Although CS_75 microparticles' cathode exhibited a high charge specific capacity of 206.5 mA h g^{-1}, its discharge capacity was observed to be 120.1 mA h g^{-1} due to the irreversible capacity loss.

After this irreversible capacity loss, the electrode showed low capacity performance as a half-cell. The long-term GCD cycle test at C/5 is shown in Fig. 11d. The CS_75 half-cell started to perform at 86 mA h g^{-1} in the first cycle and retained 77% of its capacity after 200 cycles. Despite the fact that there is still room for improvement in the optimization of the electrochemical performance of LiBs based on NMC cathodes, promising results have been obtained. In particular, after Mn-rich shell coating, improved electrode reduction voltage was achieved together with stabilized operation voltage.

4. Conclusions

In this work, NMC samples in the form of core and core–shell microparticles have been synthesized following an oxalate-assisted co-precipitation synthesis method which allows the achievement of the expected core NMC811 and core–shell NMC 811-631 compositions. XRD measurements confirm that annealing at a temperature of 750 °C is required to achieve the formation of well-crystalized NMC particles, while annealing at higher temperature promotes the segregation of the Ni-rich rock-salt phase. Additionally, XRD and Rietveld analyses indicate increased cationic Li$^+$/Ni^{2+} mixing in the particles treated at 900 °C, while the presence of a Mn-rich shell in the particles treated at 750 °C hinders Ni migration to the Li slab, which could improve their electrochemical performance in LiBs. SEM analysis reveals that the particles exhibit a homogeneous and rounded appearance within the range of 1.5–2.5 µm, with surfaces showing either a grainy or porous appearance in the core- or core–shell particles, respectively. A combination of SEM-EDS and TEM-EDS confirms the formation of a Ni-rich core–Mn-rich shell structure in the particles. *In situ* SEM analysis contributes with relevant insights into the evolution of the particles during the annealing process monitored in real time. In particular, *in situ* SEM confirms that the main volume contraction of the particles occurs at 500 °C, together with the formation of cracks at the surface of some of the annealed particles. Raman spectroscopy confirms the presence of NMC in the probed particles which exhibit dominant A$_{1g}$ and E$_g$ Raman modes related to the TM cations at 3b positions in the $R\bar{3}m$ layered structure. Deconvolution of the Raman signal reveals variations in these Raman modes among core and core–shell particles, possibly due to changes in the distance between TM cations and oxygen ions in the NMC layered structure. EDS and ICP-OES confirm the achievement of the NMC 811/631 composition, together with the successful incorporation of Li in the NMC particles. The presence of Li at the surface of the particles is further confirmed by XPS analysis, which also determines the oxidation states of the TM in the
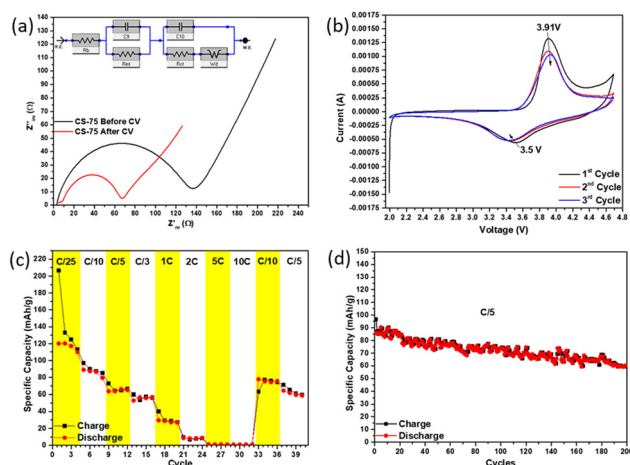

Fig. 11 Electrochemical analysis of the CS_75 sample. (a) Before CV and after CV EIS spectra comparison. (b) CV analysis. (c) C-Rate result. (d) GCD test result at 0.2C.

NMC in the core–shell particles. *In situ* XPS analysis under variable temperature and atmospheric conditions demonstrates variations in the core levels as a function of the conditions, as well as the formation of additional compounds, such as Li_2CO_3, at the surface of the particles treated at 500 °C and under an O_2 atmosphere, which can alter their electrochemical performance in LiBs. Finally, preliminary electrochemical tests have been performed in LiBs with cathodes formed by NMC core and core–shell particles treated at 750 °C. In that case, differences were observed due to the presence of a Mn-rich shell in the particles, which leads to more stabilized operation voltage and improved electrode reduction voltage stability after shell coating. There is still room for improvement, as the electrochemical behaviour of the LiBs with NMC-based cathodes can be further optimized not only with improvements in the cathode material but also by considering aspects such as the quality of the electrode prepared with NMC powders.

Author contributions

Conceptualization: J. G.-A., S. K., E. G., B. S., D. M., and B. M.; methodology: J. G.-A., S. K., E. G., B. S., D. M., and B. M.; data curation: J. G.-A., S. K., K. K., E. G., I. J. V.-G., V. P.-D., and D. M.; formal analysis: J. G.-A., S. K., E. G., B. S., I. J. V.-G., V. P.-D., D. M., and B. M.; investigation: J. G.-A., S. K., E. G., N. Y., B. S., K. K., D. M., and B. M; funding acquisition: N. Y., B. S., and B. M.; resources: B. S., E. G., N. Y., V. P.-D., D. M., and B. M.; writing – original draft: J.-G. A. and D. M.; and writing – review & editing: J. G.-A., S. K., E. G., B. S., I. J. V.-G., V. P.-D., D. M., and B. M. All authors have read and agreed to the published version of the manuscript.

Data availability

The data that support the findings of this study are available from the corresponding author upon reasonable request.

Conflicts of interest

There are no conflicts to declare.

Acknowledgements

Notes and references

1 C. M. Julien, A. Mauger, K. Zaghib and H. Groult, Comparative Issues of Cathode Materials for Li–Ion Batteries, *Inorganics*, 2014, **2**, 132–154.
2 F. Schipper, E. M. Erickson, C. Erk, J.-Y. Shin, F. F. Chesneau and D. Aurbach, Review—Recent Advances and Remaining Challenges for Lithium Ion Battery Cathodes, *J. Electrochem. Soc.*, 2017, **164**, A6220–A6228.
3 J. Xu, F. Lin, M. M. Doeff and W. Tong, A Review of Ni-Based Layered Oxides for Rechargeable Li–Ion Batteries, *J. Mater. Chem. A*, 2017, **5**(3), 874–901.
4 P. Rozier and J. M. Tarascon, Review—Li-Rich Layered Oxide Cathodes for Next-Generation Li–Ion Batteries: Chances and Challenges, *J. Electrochem. Soc.*, 2015, **162**(14), A2490–A2499.
5 X. Zhang, W. J. Jiang, A. Mauger, A. Qilu, F. Gendron and C. M. Julien, Minimization of the Cation Mixing in $Li_{1+x}(NMC)_{1-x}O_2$ as Cathode Material, *J. Power Sources*, 2010, **195**(5), 1292–1301.
6 A. Iturrondobeitia, F. Aguesse, S. Genies, T. Waldmann, M. Kasper, N. Ghanbari, M. Wohlfahrt-Mehrens and E. Bekaert, Post-Mortem Analysis of Calendar-Aged 16 A h NMC/Graphite Pouch Cells for EV Application, *J. Phys. Chem. C*, 2017, **121**(40), 21865–21876.
7 J. E. Kim and W. S. Kim, Synthesis of Core-Shell Particles of Nickel-Manganese-Cobalt Hydroxides in a Continuous Couette-Taylor Crystallizer, *Cryst. Growth Des.*, 2017, **17**(7), 3677–3686.
8 J. J. Saavedra-Arias, N. K. Karan, D. K. Pradhan, A. Kumar, S. Nieto, R. Thomas and R. S. Katiyar, Synthesis and Electrochemical Properties of $Li(Ni_{0.8}Co_{0.1}Mn_{0.1})O_2$ Cathode Material: Ex Situ Structural Analysis by Raman Scattering and X-Ray Diffraction at Various Stages of Charge–Discharge Process, *J. Power Sources*, 2008, **183**(2), 761–765.
9 C. M. Subramaniyam, H. Celio, K. Shiva, H. Gao, J. B. Goodenough, H. K. Liu and S. X. Dou, Long Stable Cycling of Fluorine-Doped Nickel-Rich Layered Cathodes for Lithium Batteries. Sustain, *Energy Fuels*, 2017, **1**(6), 1292–1298.
10 H. Lu, H. Zhou, A. M. Svensson, A. Fossdal, E. Sheridan, S. Lu and F. Vullum-Bruer, High Capacity $Li[Ni_{0.8}Co_{0.1}Mn_{0.1}]O_2$ Synthesized by Sol–Gel and Co-Precipitation Methods as Cathode Materials for Lithium-Ion Batteries, *Solid State Ionics*, 2013, **249–250**, 105–111.
11 P. Yue, Z. Wang, W. Peng, L. Li, W. Chen, H. Guo and X. Li, Spray-Drying Synthesized $LiNi_{0.6}Co_{0.2}Mn_{0.2}O_2$ and Its Electrochemical Performance as Cathode Materials for Lithium Ion Batteries, *Powder Technol.*, 2011, **214**(3), 279–282.
12 M. Jiang, Q. Zhang, X. Wu, Z. Chen, D. L. Danilov, R. A. Eichel and P. H. L. Notten, Synthesis of Ni-Rich Layered-Oxide Nanomaterials with Enhanced Li–Ion Diffusion Pathways as High-Rate Cathodes for Li–Ion Batteries, *ACS Appl. Energy Mater.*, 2020, **3**(7), 6583–6590.
13 Y. K. Sun, S. T. Myung, M. H. Kim, J. Prakash and K. Amine, Synthesis and Characterization of $Li[(Ni_{0.8}Co_{0.1}Mn_{0.1})_{0.8}(Ni_{0.5}Mn_{0.5})_{0.2}]O_2$ with the Microscale Core–Shell Structure

as the Positive Electrode Material for Lithium Batteries, *J. Am. Chem. Soc.*, 2005, **127**(38), 13411–13418.

14 Y. K. Sun, S. T. Myung, B. C. Park and K. Amine, Synthesis of Spherical Nano-To Microscale Core-Shell Particles Li[(Ni$_{0.8}$Co$_{0.1}$Mn$_{0.1}$)$_{1-x}$(Ni$_{0.5}$Mn$_{0.5}$)$_x$]O$_2$ and Their Applications to Lithium Batteries, *Chem. Mater.*, 2006, **18**(22), 5159–5163.

15 Y. Pei, Q. Chen, Y. C. Xiao, L. Liu, C. Y. Xu, L. Zhen, G. Henkelman and G. Cao, Understanding the Phase Transitions in Spinel-Layered-Rock Salt System: Criterion for the Rational Design of LLO/Spinel Nanocomposites, *Nano Energy*, 2017, **40**, 566–575.

16 S.-J. Cho, C.-C. Chung, S. Podowitz-Thomas and J. L. Jones, Understanding the Lithium Deficient Li$_x$Ni$_y$Mn$_z$Co$_{1-y-z}$O$_2$ (x < 1) Cathode Materials Structure, *Mater. Chem. Phys.*, 2019, **228**, 32–36.

17 P. Jehnichen and C. Korte, Operando Raman Spectroscopy Measurements of a High-Voltage Cathode Material for Lithium-Ion Batteries, *Anal. Chem.*, 2019, **91**(13), 8054–8061.

18 D. Liu, Z. Shadike, R. Lin, K. Qian, H. Li, K. Li, S. Wang, Q. Yu, M. Liu, S. Ganapathy, X. Qin, Q. Yang, M. Wagemaker, F. Kang, X. Yang and B. Li, Review of Recent Development of In Situ/Operando Characterization Techniques for Lithium Battery Research, *Adv. Mater.*, 2019, **31**(28), 1806620.

19 L. Shi, T. Qu, D. Liu, Y. Deng, B. Yang and Y. Dai, Process of Thermal Decomposition of Lithium Carbonate, *Miner., Met. Mater. Ser.*, 2020, 107–116.

20 H. Park, T. Yoon, Y. U. Kim, J. H. Ryu and S. M. Oh, Li$_2$NiO$_2$ as a Sacrificing Positive Additive for Lithium-Ion Batteries, *Electrochim. Acta*, 2013, **108**, 591–595.

21 S. Bak, E. Hu, Y. Zhou, X. Yu, S. D. Senanayake, S. Cho, K. Kim, K. Y. Chung, X. Yang and K. Nam, Structural Changes and Thermal Stability of Charged LiNi, *ACS Appl. Mater. Interfaces*, 2014, **6**(24), 22594–22601.

22 K. Ben-Kamel, N. Amdouni, A. Mauger and C. M. Julien, Study of the Local Structure of LiNi$_{0.33+\delta}$Mn$_{0.33+\delta}$Co$_{0.33-2\delta}$O$_2$ (0.025 ≤ δ ≤ 0.075) Oxides, *J. Alloys Compd.*, 2012, **528**, 91–98.

23 R. E. Ruther, A. F. Callender, H. Zhou, S. K. Martha and J. Nanda, Raman Microscopy of Lithium-Manganese-Rich Transition Metal Oxide Cathodes, *J. Electrochem. Soc.*, 2015, **162**(1), A98–A102.

24 N. Mironova-Ulmane, A. Kuzmin, I. Steins, J. Grabis, I. Sildos and M. Pärs, Raman Scattering in Nanosized Nickel Oxide NiO, *J. Phys.: Conf. Ser.*, 2007, **93**(1), 012039.

25 M. Taeño, J. Bartolomé, L. Gregoratti, P. Modrzynski, D. Maestre and A. Cremades, Self-Organized NiO Microcavity Arrays Fabricated by Thermal Treatments, *Cryst. Growth Des.*, 2020, **20**(6), 4082–4091.

26 C. M. Julien and M. Massot, Lattice Vibrations of Materials for Lithium Rechargeable Batteries I. Lithium Manganese Oxide Spinel, *Mater. Sci. Eng., B*, 2003, **97**(3), 217–230.

27 T. Larbi, A. Amara, B. Ouni, A. Inoubli, M. Karyaoui, A. Yumak, F. Saadallah, K. Boubaker and M. Amlouk, Physical Investigations on NiMn$_2$O$_4$ Sprayed Magnetic Spinel for

Sensitivity Applications, *J. Magn. Magn. Mater.*, 2015, **387**, 139–146.

28 X. Zhang, A. Mauger, Q. Lu, H. Groult, L. Perrigaud, F. Gendron and C. M. Julien, Synthesis and Characterization of LiNi$_{1/3}$Mn$_{1/3}$Co$_{1/3}$O$_2$ by Wet-Chemical Method, *Electrochim. Acta*, 2010, **55**(22), 6440–6449.

29 C. Ghanty, B. Markovsky, E. M. Erickson, M. Talianker, O. Haik, Y. Tal-Yossef, A. Mor, D. Aurbach, J. Lampert, A. Volkov, J. Y. Shin, A. Garsuch, F. F. Chesneau and C. Erk, Li$^+$-Ion Extraction/Insertion of Ni-Rich Li$_{1+x}$(Ni$_y$Co$_z$Mn$_z$)WO$_2$ (0.005 < x < 0.03; y: Z = 8:1, W ≈ 1) Electrodes: In Situ XRD and Raman Spectroscopy Study, *ChemElectroChem*, 2015, **2**(10), 1479–1486.

30 C. Y. Li, Z. Q. Tian, Y. Yu, C. Wang, Y. Zhang, S. Y. Zheng, J. F. Li, F. Maglia, R. Jung and Y. Shao-Horn, Surface Changes of LiNi$_x$Mn$_y$Co$_{1-x-y}$O$_2$ in Li–Ion Batteries Using in Situ Surface-Enhanced Raman Spectroscopy, *J. Phys. Chem. C*, 2020, **124**(7), 4024–4031.

31 H. J. Orman and P. J. Wiseman, Cobalt(III) Lithium Oxide, CoLiO$_2$: Structure Refinement by Powder Neutron Diffraction, *Acta Crystallogr., Sect. C: Cryst. Struct. Commun.*, 1984, **40**(1), 12–14.

32 O. Bondarchuk, A. P. LaGrow, A. Kvasha, T. Thieu, E. Ayerbe and I. Urdampilleta, On the X-Ray Photoelectron Spectroscopy Analysis of LiNi$_x$Mn$_y$Co$_z$O$_2$ Material and Electrodes, *Appl. Surf. Sci.*, 2021, **535**, 147699.

33 N. Andreu, D. Flahaut, R. Dedryvère, M. Minvielle, H. Martinez and D. Gonbeau, XPS Investigation of Surface Reactivity of Electrode Materials: Effect of the Transition Metal, *ACS Appl. Mater. Interfaces*, 2015, **7**(12), 6629–6636.

34 J. L. White, F. S. Gittleson, M. Homer and F. El Gabaly, Nickel and Cobalt Oxidation State Evolution at Ni-Rich NMC Cathode Surfaces during Treatment, *J. Phys. Chem. C*, 2020, **124**(30), 16508–16514.

35 Z. Fu, J. Hu, W. Hu, S. Yang and Y. Luo, Quantitative Analysis of Ni^{2+}/Ni^{3+} in Li[Ni$_x$Mn$_y$Co$_z$]O$_2$ Cathode Materials: Non-Linear Least-Squares Fitting of XPS Spectra, *Appl. Surf. Sci.*, 2018, **441**, 1048–1056.

36 S. Ardizzone, C. L. Bianchi and D. Tirelli, Mn$_3$O$_4$ and γ-MnOOH Powders, Preparation, Phase Composition and XPS Characterisation, *Colloids Surf., A*, 1998, **134**(3), 305–312.

37 Z. Chen, J. Wang, D. Chao, T. Baikie, L. Bai, S. Chen, Y. Zhao, T. C. Sum, J. Lin and Z. Shen, Hierarchical Porous LiNi$_{1/3}$Co$_{1/3}$Mn$_{1/3}$O$_2$ Nano-/Micro Spherical Cathode Material: Minimized Cation Mixing and Improved Li$^+$ Mobility for Enhanced Electrochemical Performance, *Sci. Rep.*, 2016, **6**(1), 1–10.

38 R. Fantin, A. Van Roekeghem and A. Benayad, Revisiting Co 2p Core-Level Photoemission in LiCoO$_2$ by in-Lab Soft and Hard X-Ray Photoelectron Spectroscopy: A Depth-Dependent Study of Cobalt Electronic Structure, *Surf. Interface Anal.*, 2023, **55**(6–7), 489–495.

39 K. N. Wood and G. Teeter, XPS on Li-Battery-Related Compounds: Analysis of Inorganic SEI Phases and a Methodology for Charge Correction, *ACS Appl. Energy Mater.*, 2018, **1**(9), 4493–4504.

40 I. A. Shkrob, J. A. Gilbert, P. J. Phillips, R. Klie, R. T. Haasch, J. Bareño and D. P. Abraham, Chemical Weathering of Layered Ni-Rich Oxide Electrode Materials: Evidence for Cation Exchange, *J. Electrochem. Soc.*, 2017, **164**(7), A1489–A1498.

41 C. Busà, M. Belekoukia and M. J. Loveridge, The Effects of Ambient Storage Conditions on the Structural and Electrochemical Properties of NMC-811 Cathodes for Li–Ion Batteries, *Electrochim. Acta*, 2021, **366**, 137358.

42 Z. Ahaliabadeh, X. Kong, E. Fedorovskaya and T. Kallio, Extensive Comparison of Doping and Coating Strategies for Ni-Rich Positive Electrode Materials, *J. Power Sources*, 2022, **540**, 231633.